

# Multistate Switching of Photonic Angular Momentum Coupling in Phase-Change Metadevices

Fei Zhang, Xin Xie, Mingbo Pu, Yinghui Guo, Xiaoliang Ma, Xiong Li, Jun Luo, Qiong He, Honglin Yu, and Xiangang Luo\*

The coupling between photonic spin and orbital angular momenta is significantly enhanced at the subwavelength scale and has found a plethora of applications in nanophotonics. However, it is still a great challenge to make such kind of coupling tunable with multiple states. Here, a versatile metasurface platform based on polyatomic phase-change resonators is provided to realize multiple-state switching of photonic angular momentum coupling. As a proof of concept, three coupling modes, namely, symmetric coupling, asymmetric coupling, and no coupling, are experimentally demonstrated at three different crystallization levels of structured  $\text{Ge}_2\text{Sb}_2\text{Te}_5$  alloy. In practical applications, coded information can be encrypted in asymmetric mode using the spin degree of freedom, while revealing misleading one without proper phase change or after excessive crystallinity. With these findings, this study may open an exciting direction for subwavelength electromagnetics with unprecedented compactness, allowing to envision applications in active nanophotonics and information security engineering.

In the past decades, artificially structured materials, such as metamaterials and metasurfaces, have attracted wide attention owing to their large degrees of freedom in realizing structured and spatially inhomogeneous optical fields.<sup>[1]</sup> In such fields, the vectorial parameters become strongly coupled with each other,<sup>[2]</sup> leading to a considerable enhancement of photonic spin-orbit interactions (PSOIs), i.e., the coupling between spin

and orbital angular momenta (SAM and OAM) of photons during the propagation of light.<sup>[3]</sup> In classical applications, PSOIs can be explained by the vectorial properties of Maxwell's equations,<sup>[4]</sup> which are also similar to the spin-orbit interaction of relativistic quantum particles<sup>[5]</sup> and electrons in solids,<sup>[6]</sup> because all of them carry SAM and OAM.<sup>[2]</sup> As such, PSOIs appear in almost all basic optical processes and provide a robust, scalable, and high-bandwidth toolbox for spin-dependent manipulation of light. Early researches on symmetric PSOIs have achieved many exotic phenomena and fantastic flat optical devices, such as broadband spin Hall effect,<sup>[7,8]</sup> full-color printing, and holography,<sup>[9,10]</sup> achromatic lenses,<sup>[11,12]</sup> ultrafast optical pulse shaping,<sup>[13]</sup> spatiotemporal light control,<sup>[14]</sup> among many others.<sup>[15–17]</sup> Current studies have aimed to

exploit the fundamental principles of basic artificial structures to realize asymmetric PSOIs<sup>[18–21]</sup> and active tunability<sup>[22–26]</sup> using the external degrees of freedom.


Asymmetric PSOIs allow the left-handed and right-handed circularly polarized (LCP and RCP) light to be independently modulated, so different information can be coded and retrieved for the two spin states. Unfortunately, the coded information can be readily decrypted by scanning the polarization states. To overcome this limitation, switchable-PSOI-based metasurfaces composed of tunable materials have been proposed to code multichannel information into different functional states.<sup>[22–26]</sup> However, the tunability of PSOIs has been demonstrated with only “ON” and “OFF” states, although a couple of demonstrations of multilevel (even up to 11 states) and fully reversible tuning of metasurfaces have been reported.<sup>[27–31]</sup> Since the information can be coded in merely “ON” state, it is unavoidable to employ interleaved subarrays to achieve multiple functions with each one contributing to only a single function, resulting in the fundamental limitations of pixel loss, information infidelity, and low energy efficiency.<sup>[17]</sup> Additionally, interlacing different subarrays also increase the period of unit cells, resulting in a dramatic loss of light to spurious diffraction orders, which may further deteriorate the information fidelity and energy efficiency.

In this work, polyatomic phase-change resonators composed of structured  $\text{Ge}_2\text{Sb}_2\text{Te}_5$  alloy (GST-225, simply GST hereafter) are employed in metasurfaces with spatially tunable

Dr. F. Zhang, Dr. X. Xie, Prof. M. Pu, Prof. Y. Guo, Prof. X. Ma, Prof. X. Li, Dr. J. Luo, Dr. Q. He, Prof. X. Luo  
State Key Laboratory of Optical Technologies  
on Nano-Fabrication and Micro-Engineering  
Institute of Optics and Electronics  
Chinese Academy of Sciences  
Chengdu 610209, China  
E-mail: lxg@ioe.ac.cn

Dr. F. Zhang, Prof. H. Yu  
Key Laboratory of Optoelectronic Technology and System  
Ministry of Education  
Chongqing University  
Chongqing 400030, China

Dr. X. Xie, Prof. M. Pu, Prof. Y. Guo, Prof. X. Ma, Prof. X. Li, Prof. X. Luo  
School of Optoelectronics  
University of Chinese Academy of Sciences  
Beijing 100049, China

 The ORCID identification number(s) for the author(s) of this article can be found under <https://doi.org/10.1002/adma.201908194>.

DOI: 10.1002/adma.201908194

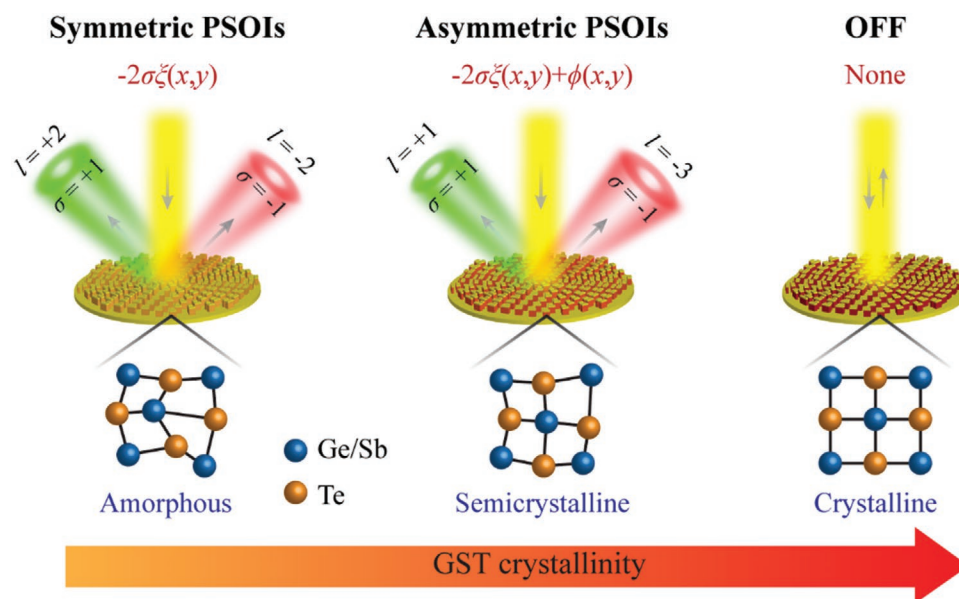


**Figure 1.** The schematic diagram of active SAM-to-OAM conversion enabled by the proposed phase-change metasurfaces. Shifting among these three modes can be realized by tuning the crystallization level of GST. It is noteworthy that the bottom schematic diagrams do not represent the real molecular structure of GST.

propagation phase combining with fixed geometric phase to realize multiple independent functions. Compared with previous interlacing designs, this fusion modulation approach shows that multiple functions can be integrated into a single phase-change metadvice without pixel loss, and affords more degrees of freedom for light manipulation. By tuning the crystallization level of GST, these functions can be switched with active tunability. As a proof-of-concept, we demonstrate symmetric, asymmetric, and “OFF” PSOIs at different crystallization levels. Meanwhile, the distinctive tunability of GST makes these coupling modes actively controllable by an appropriate thermal stimulus. Specifically, there is a mapping relationship in the space-frequency domains between symmetric and asymmetric PSOIs, which can be applied to simultaneous encodings of actual and pseudo information. Its promising applications in optical information encryption and polarization multiplexing have been experimentally demonstrated. We believe that these findings can open up new possible device concepts and find great potential in optical information storage and encryption.

**Figure 1** is a conceptual illustration of multistate switchable PSOIs enabling diverse types of SAM-to-OAM conversion by tuning the crystallization level of GST. Pseudo and actual information (e.g., the topological charges  $l$  of the OAM beam) can be coded, respectively, in symmetric and asymmetric modes combining with the spin degree of freedom. In the amorphous state, the metasurfaces are characterized by merely geometric phase (Pancharatnam–Berry phase) of  $-2\sigma\xi(x,y)$ , leading to symmetric SAM-to-OAM conversion (the signs of  $l$  are opposite for  $\sigma = \pm 1$ , where  $\sigma$  equals to  $+1$  or  $-1$  for RCP and LCP light). Therefore, only misleading information (here, it is  $l = \pm 2$ ) can be read. To decode the correct information, an appropriate stimulus is required to excite a phase transition of GST from the amorphous to an intermediate (i.e., semicrystalline) state. In this case, another propagation phase of  $\phi(x,y)$  is introduced

along with the geometric phase. The fusion of the two different types of phases allows independent control of the two opposite spin states,<sup>[18–20]</sup> resulting in the mode switching of PSOIs from symmetric to asymmetric coupling. In the asymmetric mode, two arbitrary and independent information channels (e.g.,  $l = +1, -3$ ) can be generated for the two spin states at a given crystallization level. By tuning the crystallization levels, many more states of PSOIs may be realized. Finally, if GST undergoes excessive crystallinity, PSOIs are switched into “OFF” mode, in which the incident light experiences only mirror reflection, and no valuable information can be read.

The proposed multistate switchable PSOIs can code multi-channel information, which is essentially different from previously reported functional metadvice based on dual-mode (“ON” or “OFF”) switchable PSOIs.<sup>[22–25]</sup> All elements in the presented metasurface can contribute to the wavefront control, overcoming their fundamental limitations of pixel loss and irreducible noise. More importantly, the proposed multistate switchable PSOIs have more freedoms and higher security for information encryption. For example, decoding corrective information encoded in asymmetric PSOIs requires not only a corrective incident polarization but also an appropriate stimulus to transform GST at a given crystallization level, whereas revealing misleading or useless one without proper phase change or after excessive crystallinity. This property is very important for information encryption, but it cannot be realized by previous dual-mode switchable PSOIs.<sup>[22–25]</sup> Besides, although several works have also shown the great potential of GST in active 1D wavefront modulation,<sup>[32–34]</sup> these methods originate from the discontinuity of the propagation phase in wavefronts and have no connection between the SAM and OAM. Using the propagation phase alone rarely achieves full-phase control for different functions, because it requires extremely complex designs. For example,  $n^m$  structure configurations with appropriate

dispersion are required to construct  $n^m$  phase combinations for  $m$  independent functions by  $n$  phase steps for each one,<sup>[35,36]</sup> but the fusion of the geometric phase and tunable propagation phase can reduce the total number of structure configurations from  $n^m$  to  $n^{m-1}$ , because the geometric phase can be applied to all of them in the same manner and amount.<sup>[19,20]</sup> As a result, our method may be more conducive to the design of active multifunctional metadevices.

To present the operational mechanism of the multistate switchable PSOs in metasurfaces, we first consider the optical properties of a single meta-atom. Without the loss of generality, we assume a reflective anisotropic meta-atom that can introduce phase shifts of  $\phi \pm \delta/2$  for two orthogonal polarizations along its fast and slow axes, respectively. Assuming no energy loss for simplicity, the corresponding complex amplitudes can be described as  $t_o = \exp(i\phi - i\delta/2)$  and  $t_e = \exp(i\phi + i\delta/2)$ , respectively. By performing a rotation of angle  $\xi$  with respect to the  $x$ -direction, the reflection Jones matrix  $M_r$  in Cartesian basis has the explicit form<sup>[20,37]</sup>

$$M_r = R(-\xi) \begin{bmatrix} t_o & 0 \\ 0 & t_e \end{bmatrix} R(\xi) \quad (1)$$

where

$$R(\xi) = \begin{bmatrix} \cos \xi & \sin \xi \\ -\sin \xi & \cos \xi \end{bmatrix} \quad (2)$$

is the rotation matrix. Thus, if the circularly polarized incidence of  $[1 - i\sigma]^T$  normally illuminates on the metasurface, the resulting reflected light can be written as

$$\cos \frac{\delta}{2} e^{i\phi} \begin{bmatrix} 1 \\ -i\sigma \end{bmatrix} - i \sin \frac{\delta}{2} e^{i(-2\sigma\xi + \phi)} \begin{bmatrix} 1 \\ i\sigma \end{bmatrix} \quad (3)$$

From the second term of Equation (3), it can be seen that the crosspolarized reflection component carries not only the spin-dependent geometric phase of  $-2\sigma\xi$  but also the spin-independent propagation phase of  $\phi$ . When employing an array of unit elements with identical dimensions but space-variant rotations,  $\phi$  is constant and only geometric phase contributes to the wavefront manipulation, leading to symmetric PSOs. Using various unit elements with simultaneous changes of dimensions and orientations, asymmetric PSOs are achieved through the collective contribution of the propagation and geometric phases, because  $\phi - 2\xi$  and  $\phi + 2\xi$  can be an arbitrary combination by rotating the meta-atom if  $\phi$  covers  $0-2\pi$ . However, the symmetry of PSOs is fixed once the metadevices are fabricated.

Employing phase-change materials such as GST in structure design is a proper choice to obtain a tunable propagation phase. Via appropriate thermal, optical, or electric stimulus, GST can be switched repeatedly and quickly between its amorphous and crystalline states or to be any intermediate state (a mixture of amorphous and crystalline molecules with different proportions).<sup>[38-44]</sup> Importantly, GST has a high contrast of dielectric constant at different crystallization levels (Figure S1, Supporting

Information). Therefore, the propagation phase will vary during the changing of the crystallization level, whereas the geometric phase is almost always twice the orientation angle of the meta-atom. Of course, PSOs in metasurfaces will be weakened and no valuable information can be read, if the meta-atom loses anisotropy, i.e., there is no polarization conversion and geometric phase. As a result, how to simultaneously satisfy the aforementioned conditions by a single array of unit elements is the key to realize multistate switchable PSOs, which can be achieved by properly designed polyatomic phase-change resonators.

Without losing the universality and for the sake of convenience, the design method is elaborated aiming at a wavelength of  $10.6 \mu\text{m}$ , which is the working wavelength of the  $\text{CO}_2$  laser. For a proof-of-concept demonstration, diatomic phase-change resonators sketched in Figure 2a-c are designed to implement the preceding three-state switchable PSOs. Metal-insulator-metal structure is employed to reduce the height of GST nanofins, while keeping high polarization conversion efficiency in both symmetric and asymmetric modes. Up-to-date studies show that there are catenary optical fields between two metal layers.<sup>[45]</sup> Furthermore, as its refractive index shows high contrast with that of air, the GST nanofins behave as a weakly coupled resonator. Thus, optical energy can be concentrated within different GST nanofins at different crystallization levels, which is helpful for the independent control of the geometric phase and tunable propagation phase with low crosstalk.

To excite the phase change of GST, here, thermal stimulus is employed by baking the samples on a hotplate. When the annealing time is fixed, different annealing temperatures often correspond to different crystalline levels, as long as it is higher than the phase-change temperature. In the following, the GST baked at  $\approx 185^\circ\text{C}/225^\circ\text{C}$  for 2 min is thought to be transformed into the semicrystalline/crystalline state.<sup>[39]</sup> Here, the semicrystalline state refers to the cubic phase (metastable state), and the crystalline state denotes the coexistence of the cubic and hexagonal phase, or pure hexagonal phase (stable state). Please see Section S2 in the Supporting Information for details. It should be noted that asymmetric and "OFF" modes are not limited to these two temperature steps and could also be achieved at the other two crystallization levels with proper design. For simplicity and universality, we call them semicrystalline and crystalline states.

Figure 2d-f sketches the simulated magnetic energy density distributions of one unit element at different crystallization levels under RCP illumination. One can see that the phase change from the amorphous to semicrystalline state enables energy transfer from the bigger nanofin to the smaller one (Figure 2d,e). Further being heated at the temperature of  $225^\circ\text{C}$ , GST is transformed into the crystalline state. Then, the electromagnetic wave is weakly coupled among GST nanofins and no electromagnetic resonance is observed within them, as shown in Figure 2f. In principle, these three resonant modes would lead to different amplitude/phase spectra of the crosspolarized reflection component. The optical response of the whole element is more sensitive to the size of the GST nanofin where the optical energy is concentrated. This property can guide the optimization design and help us to find desired diatomic phase-change resonators quickly.

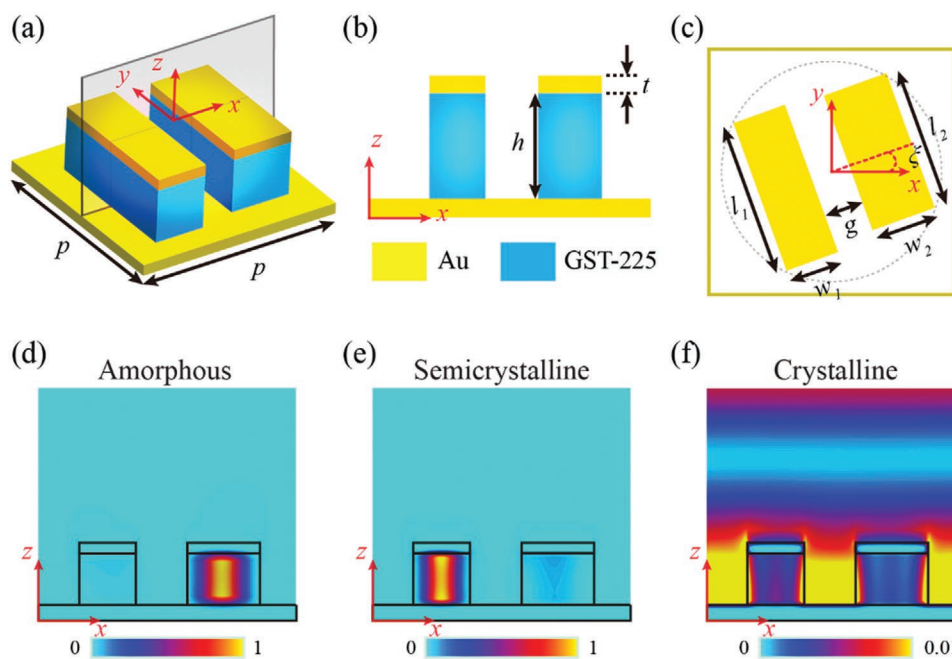


**Figure 2.** Design of diatomic phase-change resonators. a–c) 3D, side and top views of designed unit elements, showing its structural materials and geometrical parameters of  $p = 5 \mu\text{m}$ ,  $h = 1 \mu\text{m}$ , and  $t = 0.2 \mu\text{m}$ . d–f) Magnetic energy density distributions at different crystallization levels of GST on the  $xz$ -section shown in (a). The black lines denote the boundaries of structures.

We carefully designed twelve diatomic phase-change resonators with an incremental propagation phase of  $\approx \pi/6$  in the semicrystalline state between two adjacent ones but no

propagation phase difference in the amorphous state (Figure S3, Supporting Information). **Figure 3** depicts the simulated results of four designed unit elements at RCP incidence.

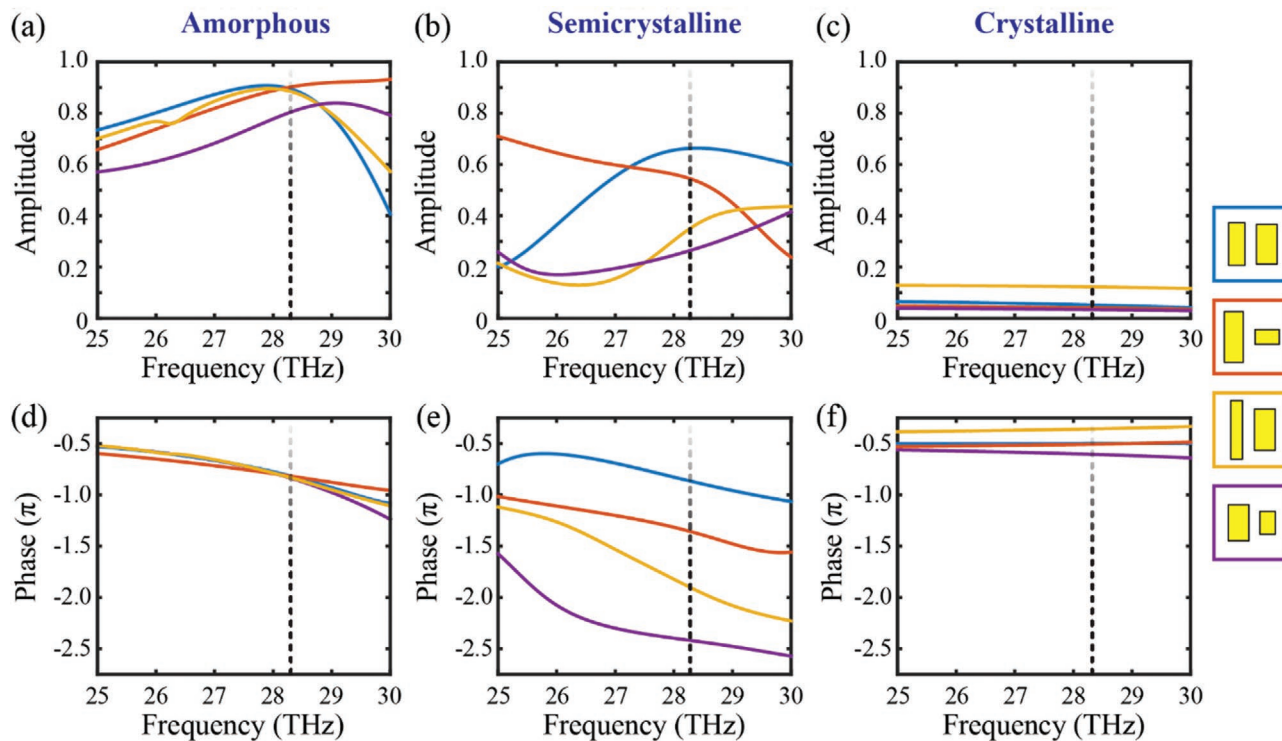


**Figure 3.** Amplitude and phase spectra of four designed unit elements. a–f) Simulated amplitude (a–c) and phase (d–f) spectra of the crosspolarized reflection component at different crystallization levels. The blue, red, orange, and purple curves, respectively, correspond to units 1, 4, 7, and 10 shown on the right side (from top to bottom).

Each colored curve corresponds to a unit element shown on the right side. In both amorphous and semicrystalline states, these unit elements support high crosspolarized amplitudes (Figure 3a,b). As we stated, there is no propagation phase difference in the amorphous state (Figure 3d), but the propagation phases covering  $0-2\pi$  are obtained in the semicrystalline state (Figure 3e). After undergoing full crystallinity, the loss of the resonator's anisotropy leads to extremely low crosspolarized amplitude (Figure 3c). More importantly, there is almost no propagation phase difference among these unit elements (Figure 3f). It means that the coded information in asymmetric coupling mode cannot be decoded in this "OFF" mode even with the help of a polarization filter and strong incident energy. Furthermore, the amplitude/phase spectra with different rotation angles are also investigated (Figure S4, Supporting Information), from which it can be found that the effect of the orientation on the amplitude is very small and the introduced geometric phase agrees well with the theoretical prediction of  $-2\sigma\xi$ .

By arranging designed twelve unit elements, multistate switchable PSOIs can be realized. We first demonstrate the active SAM-to-OAM conversion shown in Figure 1 (see Section S4 in the Supporting Information for details of design). The scanning electron microscopy (SEM) images of a fabricated converter are sketched in Figure 4a. Figure 4b–d display the measured diffraction patterns under RCP (top) and LCP (bottom) illumination at three different crystallization levels. In the amorphous and semicrystalline states, two spin components are reflected to the  $\pm 1$ st diffraction orders and present donut-shape patterns that feature OAM beams (Figure 4b,c). After excessive crystallinity, merely the central 0th tight spot originating from the copolarized component is observed even with strong incident energy (Figure 4d). With the interference of a titled circularly polarized beam (the inclined angle sets the fringe spacing), the topological charge  $l$  of generated OAM beams can be straightforwardly identified through dislocated interference fringes, as shown in Figure 4e,f. The modulus and sign of  $l$  are determined by the number and opening direction

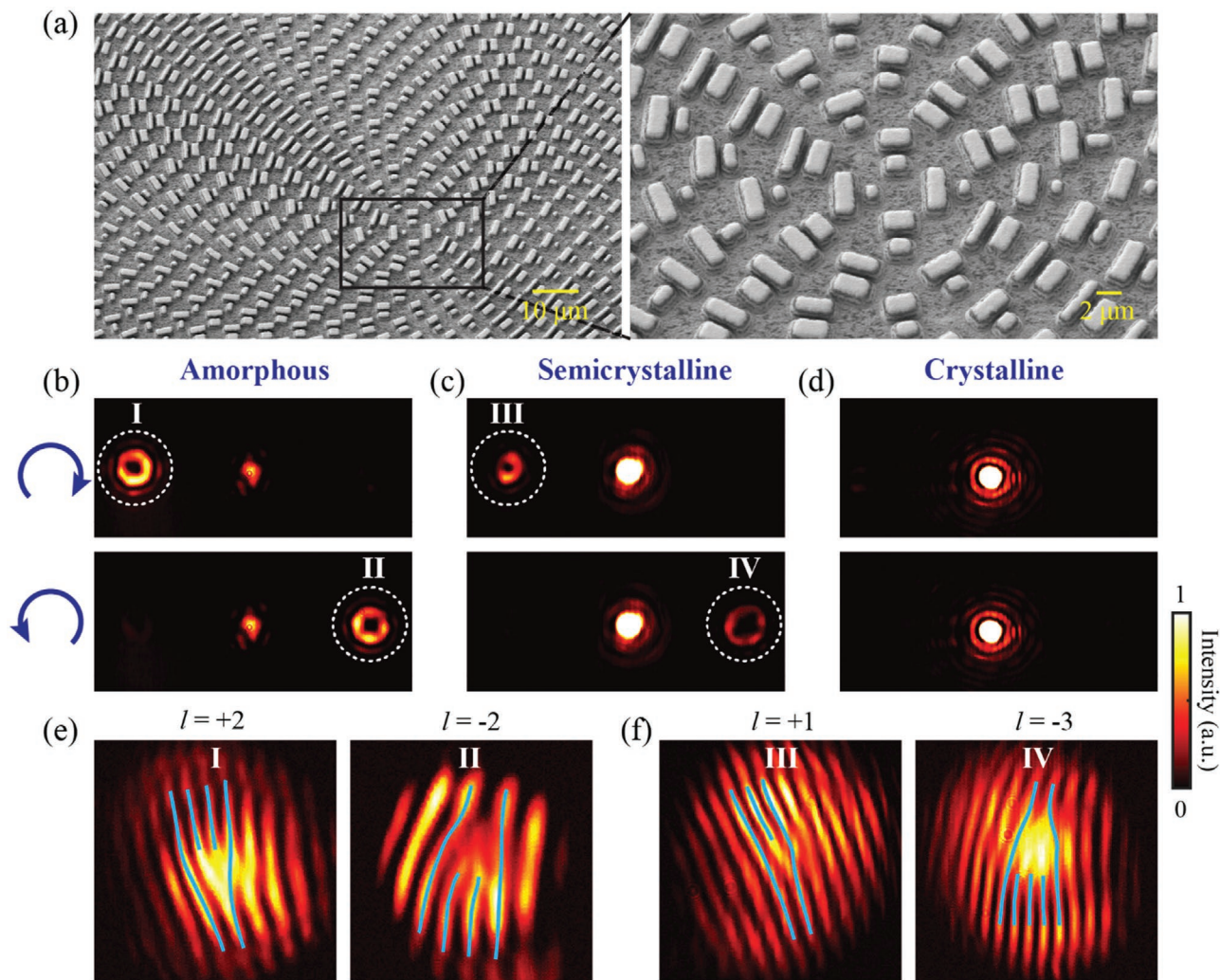


**Figure 4.** Demonstrations of active SAM-to-OAM conversion. a) SEM images of the fabricated converter. b–d) Measured diffraction patterns at different crystallization levels under RCP (top) and LCP (bottom) illumination. e,f) Interference patterns obtained through the interference of the OAM beams displayed in (b) and (c) and a titled circularly polarized Gaussian beam.

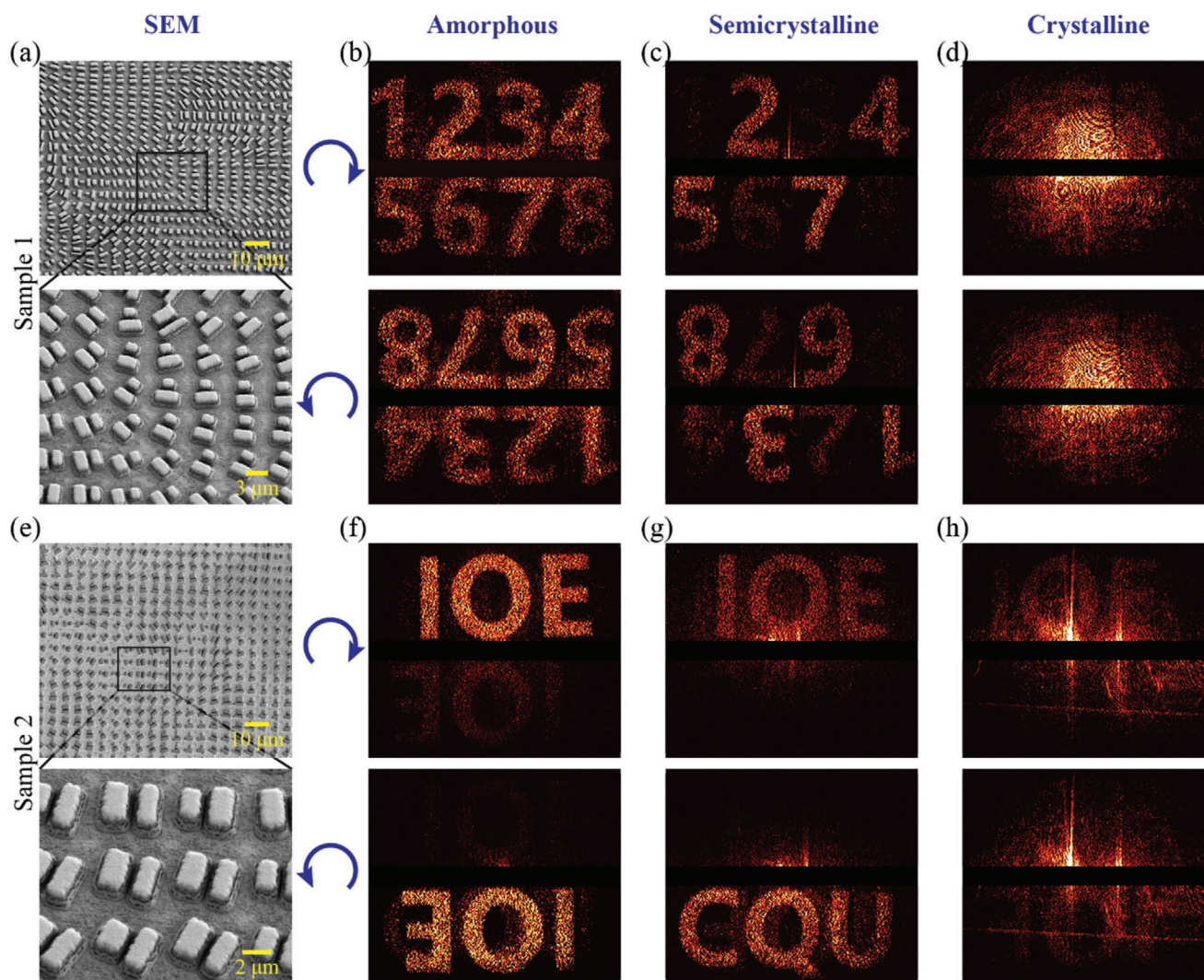


**Figure 5.** Demonstrations of optical information encryption. a, e) SEM images of two metahologram samples. b–d, f–h) Measured diffraction patterns generated by two metaholograms at different crystallization levels under RCP (top) and LCP (bottom) illumination.

of the dislocated fringes, respectively. As we predicted, the converter generates two OAM beams with opposite topological charges ( $l = \pm 2$ ) for the two spin states in the amorphous state. While in the semicrystalline state, asymmetric SAM-to-OAM conversion is realized, and  $l = +1, -3$  are obtained for the designed sample. In principle, by adjusting the propagation phase gradient, arbitrary topological charges can be realized for the two spin states (Figure S5, Supporting Information).

The abundant degrees of freedom provided by our platform allows for the implementation of PSOs in a wide variety of applications associated with optical information encryption. To demonstrate the versatility and high performance, two different phase-only metaholograms have been further designed, fabricated, and characterized (their SEM images are shown in Figure 5a, e). Two sets of independent information can be coded, respectively, at two crystallization levels or in the semicrystalline state combining with the spin degree of freedom. As a result, there are four phase distributions, namely,  $\Psi_a(x, y)$ ,  $\Psi_b(x, y)$ ,  $\Psi_c(x, y)$ , and  $\Psi_d(x, y)$  in the amorphous

and semicrystalline states with each crystallization level corresponding to two phase profiles for the two spin states, where  $\Psi_a(x, y)$  and  $\Psi_b(x, y)$  obtained by the Gerchberg–Saxton algorithm<sup>[9,10]</sup> correspond to two arbitrary and independent information channels;  $\Psi_c(x, y)$  and  $\Psi_d(x, y)$  can be calculated according to the coding mode of  $\Psi_a(x, y)$  and  $\Psi_b(x, y)$  (see Section S1 in the Supporting Information for details).

The measured diffraction patterns shown in Figure 5b–d are generated by the first metahologram. It codes  $\Psi_a(x, y)$  and  $\Psi_b(x, y)$  (e.g., corresponding to “2457” and “1368,” respectively) on the two spin components in the semicrystalline state. Then, another two phase distributions for the two spin components in the amorphous states have the explicit form of  $\Psi_{c,d}(x, y) = \pm[\Psi_a(x, y) - \Psi_b(x, y)]/2$ . As illustrated in Figure 5c, two different holographic images of “2457” and “1368” originating from asymmetric PSOs were captured under RCP and LCP illumination, respectively. However, before phase transition, two centrosymmetric patterns carrying the same information of “12345678” are obtained for the two spin states (Figure 5b),

which validates the symmetric PSOs. Such a mapping relationship in the space-frequency domains between two modes originates from the fact that the phase distributions in the symmetric PSOs are the superposition of two phase distributions coded in the asymmetric PSOs. These significant properties can be applied to optical information encryption, and the decryption requires an appropriate phase change of GST by heating the sample at a given temperature. If the thermal stimulus is excessive, i.e., GST experiences full crystallinity, no valuable information except scattering noise can be observed, as displayed in Figure 5d. It is noteworthy that the intensity of the 0th-order component is far higher than that of scattering noise.

If the goal of design is to be more secretive, there are two ways to make the information coded in the semicrystalline not appear in the amorphous state. One way is to make two holographic images coded in the asymmetric mode overlap each other in the space-frequency domain, but it lacks deception and misleading. The other way is to employ the second metahologram design that codes  $\Psi_a(x,y)$  and  $\Psi_b(x,y)$  (e.g., corresponding to “IOE” and “CQU”, respectively), for example, on the LCP component in the amorphous state and the RCP component in the semicrystalline state, respectively. Then, another two phase distributions can be calculated as  $\Psi_c(x,y) = -\Psi_a(x,y)$  and  $\Psi_d(x,y) = 2\Psi_a(x,y) + \Psi_b(x,y)$ , respectively. In the amorphous state, two centrosymmetric “IOE” patterns were captured as sketched in Figure 5f, which features the symmetric PSOs. After an appropriate phase transformation into the semicrystalline state, the superimposition of the propagation phase on the geometric phase results in the observation of “CQU” pattern under LCP illumination, as shown in the bottom panel of Figure 5g. The appearance of the weak-intensity “IOE” pattern (the top panel of Figure 5g) for another spin component is attributed to the fact that the component  $\Psi_a(x,y)$  corresponding to the “IOE” pattern plays a leading role in the superimposed phase. Furthermore, from the captured diffraction patterns (Figure 5h) in the crystalline state with stronger incident power, two centrosymmetric “IOE” patterns, which result from little crosspolarized reflection component, can be barely observed in the scattering noise. This, in turn, confirms our previous standpoint that the information coded in the semicrystalline state cannot be decoded when GST undergoes excessive crystallinity.

Multimodes switchable PSOs have been demonstrated within a relatively broad spectral region ( $\Delta\lambda/\lambda \approx 10\%$ ) (see Section S5 in Supporting Information for details). Since it is impractical to accurately measure the energy efficiency in neither vortices nor holographic patterns, another sample enabling active spin Hall effect of light has been fabricated to characterize the energy efficiency of the proposed metasurfaces (see Section S6 in the Supporting Information for details). The measured energy efficiencies are  $\approx 52\%$  and  $15\%$  in the amorphous and semicrystalline states, respectively. Lower efficiency in the semicrystalline state is attributed to the fact that the phase transition enhances the material loss. Furthermore, we also observed a 3.4%/6.9% height reduction between the amorphous and semicrystalline/crystalline GST nanofins without any noticeable changes in their lateral sizes (Figure S9, Supporting Information). Numerical simulations show that such

a subtle change rarely influences the optical performance (Figure S10, Supporting Information).

It should be noted that Au and GST will react to form AuTe<sub>2</sub> with a thickness of few nanometers during annealing.<sup>[46]</sup> For our thick GST structures with a micrometer-scale thickness, however, such a thin AuTe<sub>2</sub> layer hardly affects the performance of proposed metadevices (Figure S11, Supporting Information). To avoid this diffusion problem, the Au layer can be replaced by tungsten (W) almost without compromising the optical performance (Figure S12, Supporting Information). Objectively speaking, how to reamorphize such big-volume (micrometer-scale) GST is still an open question for future work. For reamorphization, it is necessary to study its thermal characteristics like the cooling rate and the consideration of thermally conductive layers. Additionally, it would be relatively easier to realize reamorphization if the volume of GST is compromised, for example, by applying the principle at shorter wavelengths. This work focuses on the methodology of multistate switching of photonic angular momentum coupling in phase-change metadevices. Therefore, we would expect the currently presented GST-based metadvice to have only unidirectional switching capabilities, which is enough for a proof-of-concept. The unidirectional property would be more conducive to improving security. For reversible switching capabilities, however, this methodology can also be applied to vanadium dioxide (Figure S13, Supporting Information), which is a typical volatile phase-change material and has been widely employed to construct dynamically tunable metadevices.<sup>[47,48]</sup>

In summary, we present a methodology to realize multistate switchable PSOs by employing polyatomic phase-change resonators in metasurfaces. As a proof-of-concept demonstration, symmetric, asymmetric, and “OFF” modes of PSOs are realized and actively switched with a single infrared GST metasurface. Since all unit elements contribute to the wavefront manipulation, this method could overcome the fundamental limitations of pixel loss and information infidelity faced by traditional active metadevices. Experimental results validate that the proposed multimode switching of PSOs can be applied to spin- and temperature-coded optical information storage, i.e., multiple channels of information can be coded in these different modes with abundant freedoms. Importantly, decoding actual information requires an appropriate stimulus to transform GST at a given crystallization level. Without proper phase change or after excessive crystallinity, merely misleading or scattered noise can be read. We believe that this work may open a new direction in active meta-optics, and can find wide applications in optical information encryption and storage, as well as information security engineering.

In the future study, the presented design principle could be extended to realize much more functions by increasing the structural height or adding more phase-change meta-atoms in a single unit element. To reamorphize the presented GST-based metadvice with thermal, electric, or optical stimuli, further studies on the cooling rate and compression of GST structures are required, and further considerations and adaptations of structural layers need to be embedded, for example, the inclusion of electrodes and protective layers. We envision that the concept of multistate switchable PSOs can also be implemented by the volatile phase-change material VO<sub>2</sub> for

dynamic optical-field manipulation, holding the potential for further developments and other opportunities in Engineering Optics 2.0.<sup>[49]</sup>

## Experimental Section

**Simulations:** The simulated results were obtained by employing the finite element method (FEM) in CST Microwave Studio. The unit-cell boundary conditions were applied along the  $x$  and  $y$  directions. For the  $z$ -direction, the open boundary conditions were utilized. The material parameters of gold and tungsten were from Palik's Handbook.<sup>[50]</sup> The optical constants of AuTe<sub>2</sub> and VO<sub>2</sub> were from refs. [51,52]. The dielectric functions of GST at three employed crystallization levels were from the measured results (Figure S1, Supporting Information).

**Fabrications:** The schematic diagram of the fabrication process is shown in Figure S14 in the Supporting Information. First, a silicon (Si) wafer was sequentially deposited with a 300 nm thick gold layer, a 1  $\mu$ m thick GST layer, a 350 nm thick gold layer, and a 15 nm thick silver (Ag) layer through magnetron sputtering. Then, a 150 nm thick AR-P 3170 photoresist (Pr) layer was spin-coated onto the film and baked at 100 °C for 10 min. Next, the surface plasmon (SP) lithography technique, which is one kind of super-resolution optical lithography and shows a potentially promising access to low-cost and mass nanoscale fabrication,<sup>[53]</sup> was employed to transfer the patterns from a prepared chromium (Cr) mask into the photoresist layer. The aforementioned thin Ag layer was used to amplify the evanescent waves to improve the lithography performance. The photoresist patterns were obtained by developing in the AR 300-35 for 20 s. Subsequently, the patterns were transferred into the gold film via ion beam etching (IBE) and the patterned gold layer was used as the hard-mask for the next etching procedure. Finally, the GST was etched using reactive ion etching (RIE) in the CHF<sub>3</sub> gas condition. Utilizing the SP lithography system, it was easy to fabricate the metadevices repeatedly.

**Characterizations:** The semicrystalline state was obtained by baking samples for 2 min on a hotplate, which maintains a temperature of  $\approx$ 185 °C, and the crystalline state was obtained by further annealing the sample for 2 min at  $\approx$ 225 °C. The schematic diagram of the setup employed to characterize PSOIs is shown in Figure S15 in the Supporting Information. The diffraction patterns were recorded by an infrared focal plane detector (CUBE817, Guide-Infrared Inc., 800  $\times$  600 pixels) whose pixel size was 17  $\mu$ m  $\times$  17  $\mu$ m. For efficiency measurement, the beam-expander and Fourier lens were moved away, and the infrared focal plane detector was replaced by an infrared power meter.

## Supporting Information

Supporting Information is available from the Wiley Online Library or from the author.

## Acknowledgements

F.Z., X.X., and M.P. contributed equally to this work. The authors thank all medical workers and volunteers around the world for their efforts to fight the COVID-19 virus. This work was supported by the National Natural Science Foundation of China (61975210, and 61705233).

## Conflict of Interest

The authors declare no conflict of interest.

## Keywords

Ge<sub>2</sub>Sb<sub>2</sub>Te<sub>5</sub> alloy, GST, metasurfaces, phase-change materials, spin-orbit interactions

Received: December 13, 2019

Revised: July 24, 2020

Published online: August 26, 2020

- [1] N. Yu, P. Genevet, M. A. Kats, F. Aieta, J.-P. Tetienne, F. Capasso, Z. Gaburro, *Science* **2011**, *334*, 333.
- [2] K. Y. Bliokh, F. J. Rodríguez-Fortuño, F. Nori, A. V. Zayats, *Nat. Photonics* **2015**, *9*, 796.
- [3] V. S. Liberman, B. Y. Zel'Dovich, *Phys. Rev. A* **1992**, *46*, 5199.
- [4] K. Y. Bliokh, M. A. Alonso, E. A. Ostrovskaya, A. Aiello, *Phys. Rev. A* **2010**, *82*, 063825.
- [5] A. I. Akhiezer, V. B. Berestetskii, *Quantum Electrodynamics*, Interscience Publishers, New York **1965**.
- [6] D. Xiao, M.-C. Chang, Q. Niu, *Rev. Mod. Phys.* **2010**, *82*, 1959.
- [7] X. Luo, M. Pu, X. Li, X. Ma, *Light: Sci. Appl.* **2017**, *6*, e16276.
- [8] Y. Liu, Y. Ke, H. Luo, S. Wen, *Nanophotonics* **2017**, *6*, 51.
- [9] X. Li, L. Chen, Y. Li, X. Zhang, M. Pu, Z. Zhao, X. Ma, Y. Wang, M. Hong, X. Luo, *Sci. Adv.* **2016**, *2*, e1601102.
- [10] F. Zhang, M. Pu, P. Gao, J. Jin, X. Li, Y. Guo, X. Ma, J. Luo, H. Yu, X. Luo, *Adv. Sci.* **2020**, *7*, 1903156.
- [11] S. Wang, P. C. Wu, V.-C. Su, Y.-C. Lai, M.-K. Chen, H. Y. Kuo, B. H. Chen, Y. H. Chen, T.-T. Huang, J.-H. Wang, R.-M. Lin, C.-H. Kuan, T. Li, Z. Wang, S. Zhu, D. P. Tsai, *Nat. Nanotechnol.* **2018**, *13*, 227.
- [12] W. T. Chen, A. Y. Zhu, V. Sanjeev, M. Khorasaninejad, Z. Shi, E. Lee, F. Capasso, *Nat. Nanotechnol.* **2018**, *13*, 220.
- [13] S. Divitt, W. Zhu, C. Zhang, H. J. Lezec, A. Agrawal, *Science* **2019**, *364*, 890.
- [14] A. M. Shaltout, K. G. Lagoudakis, J. van de Groep, S. J. Kim, J. Vuckovic, V. M. Shalaev, M. L. Brongersma, *Science* **2019**, *365*, 374.
- [15] X. Ma, M. Pu, X. Li, Y. Guo, X. Luo, *Opto-Electron. Adv.* **2019**, *2*, 180023.
- [16] X. Xie, X. Li, M. Pu, X. Ma, K. Liu, Y. Guo, X. Luo, *Adv. Funct. Mater.* **2018**, *28*, 1706673.
- [17] N. A. Rubin, G. D'Aversa, P. Chevalier, Z. Shi, W. T. Chen, F. Capasso, *Science* **2019**, *365*, eaax1839.
- [18] R. C. Devlin, A. Ambrosio, N. A. Rubin, J. P. B. Mueller, F. Capasso, *Science* **2017**, *358*, 896.
- [19] J. P. Balthasar Mueller, N. A. Rubin, R. C. Devlin, B. Groever, F. Capasso, *Phys. Rev. Lett.* **2017**, *118*, 113901.
- [20] F. Zhang, M. Pu, J. Luo, H. Yu, X. Luo, *Opto-Electron. Eng.* **2017**, *44*, 319.
- [21] F. Zhang, M. Pu, X. Li, P. Gao, X. Ma, J. Luo, H. Yu, X. Luo, *Adv. Funct. Mater.* **2017**, *27*, 1704295.
- [22] C. Choi, S. Y. Lee, S. E. Mun, G. Y. Lee, J. Sung, H. Yun, J. H. Yang, H. O. Kim, C. Y. Hwang, B. Lee, *Adv. Opt. Mater.* **2019**, *7*, 1900171.
- [23] J. Li, S. Kamin, G. Zheng, F. Neubrech, S. Zhang, N. Liu, *Sci. Adv.* **2018**, *4*, eaar6768.
- [24] X. Yin, T. Steinle, L. Huang, T. Taubner, M. Wuttig, T. Zentgraf, H. Giessen, *Light: Sci. Appl.* **2017**, *6*, e17016.
- [25] M. Zhang, M. Pu, F. Zhang, Y. Guo, Q. He, X. Ma, Y. Huang, X. Li, H. Yu, X. Luo, *Adv. Sci.* **2018**, *5*, 1800835.
- [26] A. Nemati, Q. Wang, M. Hong, J. Teng, *Opto-Electron. Adv.* **2018**, *1*, 180009.
- [27] J. Tian, H. Luo, Y. Yang, F. Ding, Y. Qu, D. Zhao, M. Qiu, S. I. Bozhevolnyi, *Nat. Commun.* **2019**, *10*, 396.
- [28] C. Ruiz de Galarreta, I. Sinev, A. M. Alexeev, P. Trofimov, K. Ladutenko, S. Garcia-Cuevas Carrillo, E. Gemo, A. Baldycheva, J. Bertolotti, C. David Wright, *Optica* **2020**, *7*, 476.



- [29] A. U. Michel, A. Hessler, S. Meyer, J. Pries, Y. Yu, T. Kalix, M. Lewin, J. Hanss, A. De Rose, T. W. W. Mass, M. Wuttig, D. N. Chigrin, T. Taubner, *Adv. Mater.* **2019**, *31*, 1901033.
- [30] A. Leitis, A. Hefßler, S. Wahl, M. Wuttig, T. Taubner, A. Tittl, H. Altug, *Adv. Funct. Mater.* **2020**, *30*, 1910259.
- [31] J. Jang, K. Kang, N. Raeis-Hosseini, A. Ismukhanova, H. Jeong, C. Jung, B. Kim, J. Y. Lee, I. Park, J. Rho, *Adv. Opt. Mater.* **2020**, *8*, 1901932.
- [32] R. de Galarreta Carlota, M. Alexeev Arseny, Y.-Y. Au, M. Lopez-Garcia, M. Klemm, M. Cryan, J. Bertolotti, C. D. Wright, *Adv. Funct. Mater.* **2018**, *28*, 1704993.
- [33] H. Chu Cheng, L. Tseng Ming, J. Chen, C. Wu Pin, Y.-H. Chen, H.-C. Wang, T.-Y. Chen, T. Hsieh Wen, J. Wu Hui, G. Sun, P. Tsai Din, *Laser Photonics Rev.* **2016**, *10*, 986.
- [34] Y. Chen, X. Li, Y. Sonnefraud, A. I. Fernández-Domínguez, X. Luo, M. Hong, S. A. Maier, *Sci. Rep.* **2015**, *5*, 8660.
- [35] E. Arbabi, A. Arbabi, S. M. Kamali, Y. Horie, A. Faraon, *Opt. Express* **2016**, *24*, 18468.
- [36] Z. Shi, M. Khorasaninejad, Y. W. Huang, C. Roques-Carmes, A. Y. Zhu, W. T. Chen, V. Sanjeev, Z. W. Ding, M. Tamagnone, K. Chaudhary, R. C. Devlin, C. W. Qiu, F. Capasso, *Nano Lett.* **2018**, *18*, 2420.
- [37] M. Pu, X. Li, X. Ma, Y. Wang, Z. Zhao, C. Wang, C. Hu, P. Gao, C. Huang, H. Ren, X. Li, F. Qin, J. Yang, M. Gu, M. Hong, X. Luo, *Sci. Adv.* **2015**, *1*, e1500396.
- [38] F. Ding, Y. Yang, S. I. Bozhevolnyi, *Adv. Opt. Mater.* **2019**, *7*, 1801709.
- [39] A. Sarangan, J. Duran, V. Vasilyev, N. Limberopoulos, I. Vitebskiy, I. Anisimov, *IEEE Photonics J.* **2018**, *10*, 2200409.
- [40] M. Wuttig, H. Bhaskaran, T. Taubner, *Nat. Photonics* **2017**, *11*, 465.
- [41] N. Raeis-Hosseini, J. Rho, *Appl. Sci.* **2019**, *9*, 564.
- [42] N. Raeis-Hosseini, S. Lim, H. Hwang, J. Rho, *Adv. Electron. Mater.* **2018**, *4*, 1800360.
- [43] N. Raeis-Hosseini, J. Rho, *Materials* **2017**, *10*, 1046.
- [44] A. Nemat, Q. Wang, M. Hong, J. Teng, *Opto-Electron. Adv.* **2018**, *1*, 18000901.
- [45] X. Luo, *Catenary Optics*, Springer, Singapore **2019**.
- [46] L. Lu, W. Dong, J. K. Behera, L. Chew, R. E. Simpson, *J. Mater. Sci.* **2019**, *54*, 2814.
- [47] T. Badloe, I. Kim, J. Rho, *Sci. Rep.* **2020**, *10*, 4522.
- [48] S. J. Kim, I. Kim, S. Choi, H. Yoon, C. Kim, Y. Lee, C. Choi, J. Son, Y. W. Lee, J. Rho, B. Lee, *Nanoscale Horiz.* **2020**, *5*, 1088.
- [49] X. Luo, *Engineering Optics 2.0: A Revolution in Optical Theories, Materials, Devices and Systems*, Springer, Singapore **2019**.
- [50] E. D. Palik, *Handbook of Optical Constants of Solids II*, Academic Press, Boston, MA **1991**.
- [51] P. H. M. van Loosdrecht, A. M. Gerrits, K. Balzuweit, W. Konig, A. Wittlin, P. J. M. van Bentum, *J. Phys.: Condens. Matter* **1993**, *5*, 3977.
- [52] J. A. Coath, M. A. Richardson, *Proc. SPIE* **1999**, 3738, 555.
- [53] P. Gao, N. Yao, C. Wang, Z. Zhao, Y. Luo, Y. Wang, G. Gao, K. Liu, C. Zhao, X. Luo, *Appl. Phys. Lett.* **2015**, *106*, 093110.